IEEE Access
Multidisciplinary | Rapid Review | Open Access Journal

Received 31 July 2022, accepted 20 August 2022, date of publication 25 August 2022, date of current version 2 September 2022.

Digital Object Identifier 10.1109/ACCESS.2022.3201502

RESEARCH ARTICLE

Electromagnetic Signal Modulation by Chromatic Dispersion in Phase Gradient Metasurface

YUEYU MENG[1], JIAFU WANG[1], (Member, IEEE), WEIYU WANG[1], LIN ZHENG[2], YONGFENG LI[1], HUA MA[1], AND SHAOBO QU[1]

[1]Fundamentals Department, Air Force Engineering University, Xi'an, Shaanxi 710051, China
[2]School of Information and Communications Engineering, Xi'an Jiaotong University, Xi'an 710049, China

Corresponding authors: Hua Ma (mahuar@mail.xjtu.edu.cn) and Shaobo Qu (qushaobo@mail.xjtu.edu.cn)

This work was supported in part by the National Natural Science Foundation of China under Grant 61901508, Grant 61971435, and Grant 61971437.

ABSTRACT Chromatic dispersion in phase gradient metasurface and its impact on the scattered electromagnetic signals are studied in this paper. Due to its intrinsic material dispersion and special spatial arrangement of unit cells, phase gradient metasurfaces produce large chromatic dispersion for the scattering waves, resulting in anomalous reflection and refraction phenomena. Moreover, from the perspective of signal domain, the scattered waves no longer carry the whole information of the incident wave, especially for the wideband ones, because different frequencies are scattered into different directions due to the large chromatic dispersion. This progress is equivalent to a signal modulation in each scattering direction. Here we utilized a simple calculation method to achieve the direction-related spectral response characteristic for a given metasurface using 2D Fourier transform of the 2D phase pattern. Furthermore, a typical wideband radar signal was adopted to give a visualized display of the modulation effect. The simulated results showed that the scattered signals were greatly distorted, causing the correlation reduction and range deviation in radar detection. This work opens a new possibility for metasurface to manipulate the signal characteristic of electromagnetic waves and may prompt new applications in antennas, communication and radar systems

INDEX TERMS Chromatic dispersion, phase gradient metasurface, signal modulation, wideband radar.

I. INTRODUCTION

Over the past few years, artificial metasurfaces have attracted much attention in the field of electromagnetic (EM) wave manipulation, including amplitude, polarization, phase and wavefront [1], [2], [3], [4], [5]. Among them, phase gradient metasurfaces (PGMs) [6], composed of subwavelength unit cells with special spatial phase distribution, were developed to manipulate the directions of refracted/reflected waves. According to generalized laws of reflection and refraction, derived by Yu *et al.* [7], [8], a series of applications were exploited, such as antennas [9], [10], [11], cloaks [12], [13], surface wave couplers [14], [15], nonreciprocal devices [16], and wireless communications [17]. These applications concern mainly about the waves' propagation direction in the effect of anomalous reflection and refraction. However, one basic function of microwaves is transmitting information, to the best of our knowledge, seldom study pay attention to the influence on the signal or information carried by the microwave.

Chromatic dispersion spatially separates white light into different colors, which is an ancient and modern topic in the history of optical science. There are two types of classical chromatic dispersion: refractive elements, such as triangular glass prisms, exhibit dispersion due to their frequency-related refractive indices; diffractive gratings and flat lenses operates inherent to the diffraction phenomenon [18], [19]. Chromatic dispersions are detrimental in imaging systems, but indispensable in some optical systems such as spectrometer [20]. Metasurfaces have played an important role in chromatic dispersion engineering, promoting many achievements in chromatic aberration control [21], [22] and achromatic lenses [23], [24], [25]. For the PGMs, the notably chromatic dispersion is associated with the anomalous reflection

The associate editor coordinating the review of this manuscript and approving it for publication was Xinxing Zhou.

and refraction, which is due to the special spatial arrangement and the resonant phase dispersion of artificial structures. Especially for the wideband ones [26], [27], [28], the reflection angle discrepancy decomposed in a more wide spatial range. It is worth noting that large chromatic dispersion has an impact on the signal characteristic of the deflected waves [29], [30], [31], [32].

In this paper, we focus on the signal characteristic modulation of chromatic dispersion in the PGMs. For the incident EM signal with a wide frequency range, different frequency components will be deflected into different directions by PGMs. Thus for the receivers in different directions, they will get signals with different spectral characteristics. Based on the spatial 2D Fourier transform frequency, we got the direction-related spectral response characteristic. We further show that the signal modulation by PGM's chromatic dispersion will lead to a strong distortion of wideband radar signals, both for the bistatic and monostatic scattered waves. It may have potential applications in the radar systems and related.

II. CHROMATIC DISPERSION IN PHASE GRADIENT METASURFACE

We present a schematic illustration to the chromatic dispersion in PGM, as shown in Fig. 1. According to the basic principle of generalized Snell's Laws of reflection, taking the simple normal incidence as an example, the direction of the reflected wave can be calculated as [7]

$$\theta_r = \arcsin\left(\frac{c}{2\pi f}\frac{d\Phi}{dx}\right) \tag{1}$$

in which θ_{r} is the angle of reflection, c is the speed of light in air, f is the frequency of the EM wave, and $d\Phi/dx$ is the phase gradient of the metasurface. It can be seen obviously that for those metasurface with fixed phase gradient the angle of reflection is related to the frequency of the EM wave. For this reason, if the metasurface is illumined by a wideband EM wave with frequency range from $f_{\min}$ to $f_{\max}$, then the reflected waves with different frequencies will be scatted into different directions. It just likes the chromatic refraction in triple prism or the diffraction in gratings, that a beam of white light is split into the various colors of the spectrum. Thus the receivers at different directions get only a small part of the whole spectrum, which contains incomplete information of the transmitter.

Now we turn to the analytically calculation of the spectral characteristics of the reflected waves on different directions. We consider a general metasurface with $M \times N$ array of unit cells. It can be considered as a passive array antenna and the unit cells as sub-array antennas. When it is illuminated by normally plane wave incident EM wave, the far-field scattering function can be expressed as [33]

$$F(\theta, \varphi) = f_{m,n}(\theta, \varphi) S_a(\theta, \varphi) \tag{2}$$

where θ and φ are the elevation and azimuth angles of the reflected wave. $f_{m,n}(\theta, \varphi)$ is the primary pattern which expresses the vector properties of far-field polarization and directional pattern. It can be achieved from the simulation of the single unit cell. Due to the deep subwavelength property of the unit cell, whose scattering can be regarded as a homogeneous subwavelength reflector, the primary pattern $f_{m,n}(\theta, \varphi)$ is approximately identical in all the directions.

$S_a(\theta, \varphi)$ is the array pattern, for incidence with elevation angle θ_i and azimuth angle φ_i, it can be expressed as

$$S_a(\theta, \varphi) = \sum_{m=1}^{M}\sum_{n=1}^{N} \mathrm{e}^{j\psi_{m,n}} \mathrm{e}^{jp_x(m-\frac{1}{2})(k_{xr}-k_{xi})} \mathrm{e}^{jp_y(n-\frac{1}{2})(k_{yr}-k_{yi})} \tag{3}$$

where $\psi_{m,n}$ is the reflection phase of each element, p_x and p_y are the size of the unit cell in x direction and y direction, $k_{xr}(k_{yr})$ and $k_{xi}(k_{yi})$ are the component of wave vector of reflected and incident waves in the direction of the $x(y)$ axis, they can be calculated as

$$\begin{aligned} k_{xr} &= k_0 \sin\theta_r \cos\varphi_r, \quad k_{xi} = k_0 \sin\theta_i \cos\varphi_i \\ k_{yr} &= k_0 \sin\theta_r \sin\varphi_r, \quad k_{yi} = k_0 \sin\theta_i \sin\varphi_i \end{aligned} \tag{4}$$

where k_0 is the value of free space wave vector, θ_r and φ_r are the elevation angle and azimuth angle of the reflected wave. Expanding the polynomial on the exponential function and merging them again, equation (3) can be transformed as

$$\begin{aligned} S_a(k_{xr}, k_{yr}) = \mathrm{e}^{-j\frac{p_x k_{xr}}{2} - j\frac{p_y k_{yr}}{2}} \sum_{m=1}^{M}\sum_{n=1}^{N} \mathrm{e}^{j\psi(m,n)} \\ \times \mathrm{e}^{jmp_x(k_{xr}-k_{xi})} \mathrm{e}^{jnp_y(k_{yr}-k_{yi})} \end{aligned} \tag{5}$$

Particularly, for the situation of normal incidence, function (5) can be rewritten as

$$\begin{aligned} S_a(k_{xr}, k_{yr}) = \mathrm{e}^{-j\frac{p_x k_{xr}}{2} - j\frac{p_y k_{yr}}{2}} \sum_{m=1}^{M}\sum_{n=1}^{N} \mathrm{e}^{j\psi(m,n)} \\ \times \mathrm{e}^{j(mp_x k_{xr} + np_y k_{yr})} \end{aligned} \tag{6}$$

Now the function is simplified to a double summation on the metasurface with $M \times N$ cells. The double summation operation in equation (6) is actually a calculation of 2D inverse discrete Fourier transform (IDFT) [34] for the variable $\psi_{m,n}$. In fact, the calculation of $S_a(k_{xr}, k_{yr})$ for arbitrary incident direction can be achieved through 2D IDFT [35]. Look back to equation (5), it also represents a 2D IDFT calculation, with a small difference that it has translations of spatial frequency k_{xi} and k_{yi} in k_x and k_y directions, respectively.

To clearly illustrate the working mechanism of the function, we take a simple coding metasurface [36] as an example, which is consist with two types cells with a phase difference of 180° alternately arranged as a chess board form, as shown in Fig. 2(a). Fig. 2(b) shows the 2D IDFT result of the phase pattern $\psi_{m,n}$, which reveals the energy distribution in the $\boldsymbol{k}$ space and the scattering characteristic. It's obvious that the scattering pattern in the far-field can be expressed by the coordinates (θ, φ) by making a coordinate transformation from (k_x, k_y) to (θ, φ) according to equation (4), and the 3D far-field scattering patterns result is shown in Fig. 2(c).

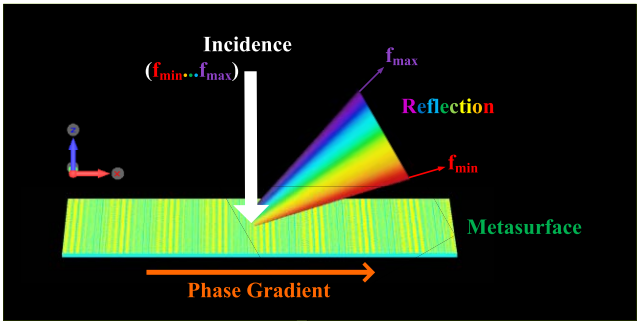

FIGURE 1. Schematic illustration of the chromatic dispersion in PGM.

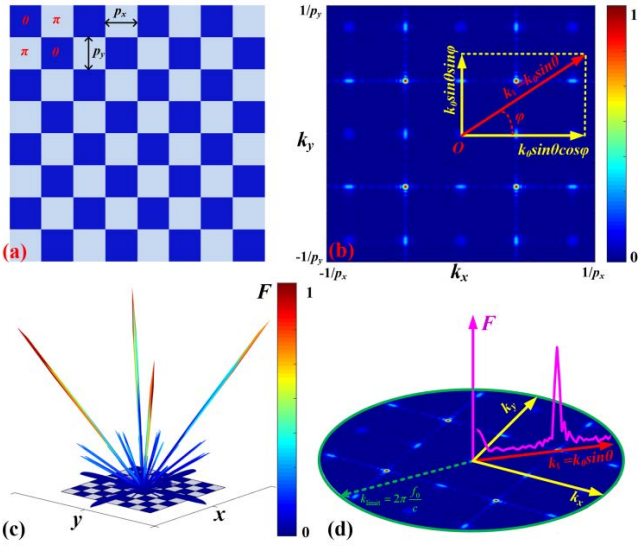

FIGURE 2. (a) Phase distribution of the coding metasurface. (b) 2D DFT result of the phase pattern. (c) The 3D far-field scattering pattern plotted in the spherical coordinate system. (d) Radiating area on the k-space (range within the green circle) and the spectral characteristics (magenta curve) of the reflected waves on $\varphi = 45°$.

Furthermore, from the 2D IDFT results we can get the spectral characteristics for an arbitrary given direction with azimuth angle φ and elevation angle θ. As the red arrow shown in Fig. 2(b), marked as $\boldsymbol{k}_{||}$, it equals $\boldsymbol{k_0}\mathbf{sin}\theta$ and represents the component projected into the horizontal plane from the space reflection wave vector whose numerical value is k_0. Moreover, the azimuth angle φ of the wave vector component $\boldsymbol{k}_{||}$ in the $\boldsymbol{k}$ space is just corresponding to the azimuth angle φ of the reflected wave in free space. Thus, the scattering spectral characteristics is corresponding to the 2D IDFT result for the same azimuth angle φ, just picking up the IDFT results along the red wave vector. And furthermore, for a given elevation angle θ, the wave vector $\boldsymbol{k}_{||} = k_0 \sin\theta = 2\pi f_0 \sin\theta/c$, is proportionate to the wave frequency f_0. Thus, taking $\boldsymbol{k}_{||}$ as abscissa, the IDFT results as the ordinate, we get an amplitude response curve for one specific azimuth angle φ, as the magenta curve shown in Fig. 2(d). Another dimension of amplitude response names F was added in Fig. 2(d) based on Fig. 2(b), which is a three-dimensional image. The horizontal plane is the $\boldsymbol{k}$ space with the same IDFT results to Fig. 2(b). The ordinate value of the magenta curve is right the IDFT result. If different $\boldsymbol{k}_{||}$ is chosen, different spectral response curves can be achieved. And using the proportional relation between $\boldsymbol{k}_{||}$ and f_0, the abscissa can be changed into frequency f_0 under a given elevation angle θ. In this way, the spectral response of the reflected waves on specific directions (θ, φ) was got.

It should be noted that the wave vector $\boldsymbol{k}_{||}$ has the upper bound of k_{0f}, the wave vector beyond k_0 in $\boldsymbol{k}$ space will not correspond to any reflected wave in free space. So the whole visible range in$\boldsymbol{k}$ space is the inner area of the green circle with the radius $k_{\text{limit}} = 2\pi f_0/c$, as shown in Fig. 2(d). Obviously, the circle's size varies with frequencies.

III. PHASE GRADIENT METASURFACE DESIGN

A wideband signal is conducive to achieve an obvious chromatic dispersion effect. Here a co-polarization reflective unit cell under circular polarization (CP) wave incidence is employed to compose the PGM, using Pancharatnam–Berry (PB) geometrical phase to achieve a wideband response. In this work, the unit cell is composed of an N-shaped structure etched on a dielectric substrate ($\varepsilon_r = 2.65$, loss tangent is 0.01) with a metallic ground, as shown in Fig. 3(a). The metallic structure on top is constituted of copper with a thickness of 0.036mm. The unit cell has a period of $p = 50.0$mm, and the other geometrical parameters are as follow: $a = 35.0$mm, $b = 47.5$mm, $d = 30.0$mm, $w_1 = 2.0$mm and $w_2 = 3.0$mm.

The reflectivity under left-handed circular polarization (LCP) and right-handed circular polarization (RCP) waves normal incidence was calculated using commercial software CST Microwave Studio. Figure 3(b) gives the simulated results in the frequency range of 0.1–3.0 GHz, where r_{LL}/r_{RR} and r_{RL}/r_{LR} represent the co- and cross polarization reflectivity under LCP and RCP incidences, respectively. The results demonstrate the unit cell's high-efficiency, wideband co-polarization reflection under CP waves' incidence.

Based on the principle of Pancharatnam-Berry (PB) phase [33], [37], the reflection phase can be modulated though rotating the metallic structure around its center. A unit cell with a rotation angle α will generate a reflection phase shift of $\pm 2\alpha$, where "+" is for LCP wave, "−" is for RCP wave. As shown in Fig. 4(b), 8 metallic structures with different rotation angle α were adopted to form a super cell of the PGM. The rotation angles have a step of 22.5°. Fig. 4(c) and (d) show the co-polarization reflection amplitude and phase of the 8 unit cells for LCP incidence. It's clear that, as the rotation angle α varied from 0° to 157.5°, the amplitude are all larger than 0.96 from 0.85 to 1.84GHz, but the phase increased with a step of about 45° in the whole frequency range. So the amplitude responses of different unit cells can be regarded as normalizes values in the theoretical calculation of far-field scattering, and the phase responses can be regarded as linear change.

To give a variation of the approximate treatment, we make a contrastive analysis of the theoretical calculation and

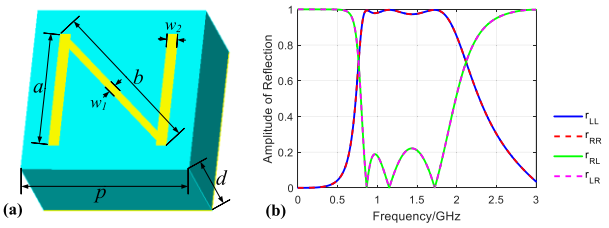

FIGURE 3. (a) Structure design of the unit cell. (b) Simulated reflection amplitude.

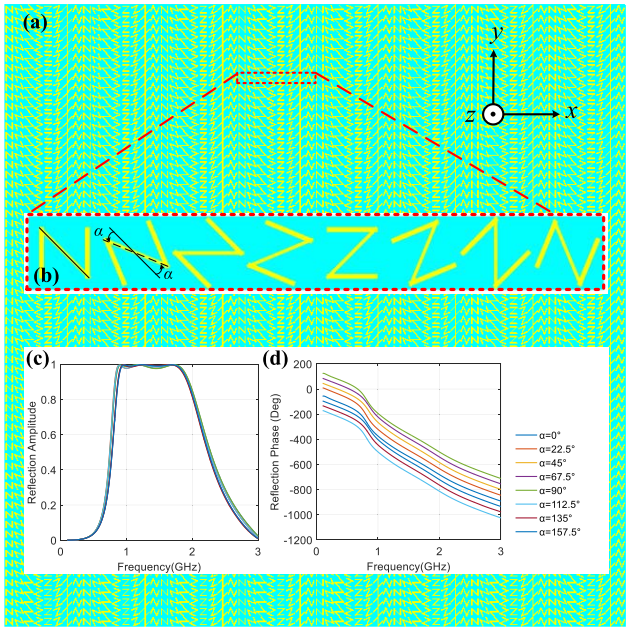

FIGURE 4. (a) The whole structure of the PGM consists of 64 × 64 unit cells (or 8 × 64 super cells). (a)Super cell design of the PGM. (b)Simulated co-polarization reflection amplitude and (c) phase of the 8 unit cells for LCP incidence.

simulation in CST Microwave Studio. In the simulation, a PGM structure consist of 64 × 64 unit cells (or 8 × 64 super cells) illuminated under LCP waves was modeled, as shown in Fig. 4(a). The normalized 3D far-field scattering patterns under normal incidence at frequencies of 0.9GHZ, 1.2GHz and 1.5GHz are simulated and monitored, as shown in Fig. 5 (a), (c) and (e), respectively. The corresponding 2D far-field scattering patterns are depicted in blue solid lines, as shown in Fig. 5(b), (d) and (f), respectively. The simulation results shown that the elevation angles of the anomalous scattered main lobe are respectively 56.5°, 35.8° and 30.0°, which is in accord with the phase gradient design.

Using the above mentioned theoretical calculation method, the 2D IDFT of the phase distribution $\psi_{m,n}$ of the same size metasurface (64 × 64 unit cells) was calculated, as shown in Fig. 6(a). According to the phase gradient design along the x-axis, $\nabla\varphi = (\pi/4)/p = 15.7\ \mathrm{m}^{-1}$, this value is corresponding to the location of the bright point at $(k_x, k_y) = (15.7, 0)\ \mathrm{m}^{-1}$ in Fig. 6(a). After transforming the coordinate of the 2D IDFT results within the circles areas (the three dashed circles in Fig. 6(a)) from (k_x, k_y) to (θ, φ), the far-field scattering pattern in for three different frequencies 0.9GHz, 1.2GHz and 1.5GHz can be got. The calculated corresponding 2D far-field scattering patterns are depicted in red dashed lines, as shown in Fig. 5(b), (d) and (f), respectively. It is clear that the calculation results of the main lobe scattering is nearly the same as the simulation results. And it's worth noting that due to the non-ideality of the amplitude and phase response of the actual unit cells in the metasurface structure, the side lobe is enhanced significantly compared to the theoretical calculation results. Because the chromatic dispersion is companied with the main lobe, so the deviation in side lobe provided little impact on the signal modulation effect.

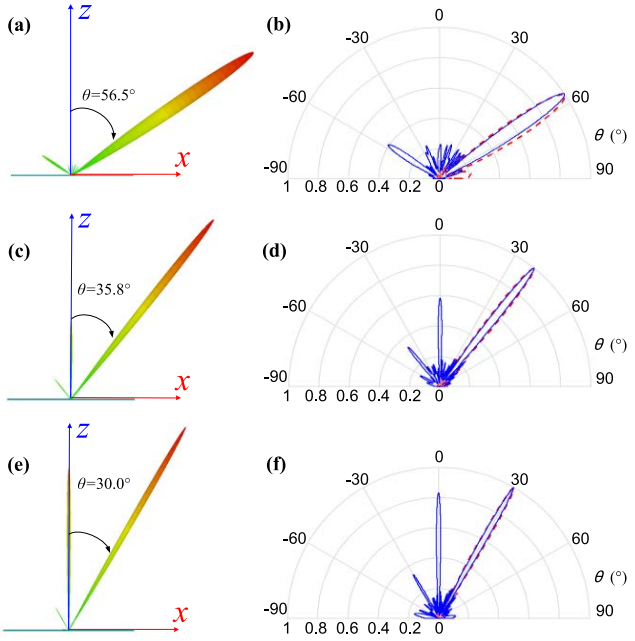

FIGURE 5. The normalized 3D and 2D far-field scattering patterns at frequencies of (a-b) 0.9GHZ, (c-d) 1.2GHz and (e-f) 1.5GHz. The elevation angles of the main lobe are 56.5°, 35.8° and 30.0°, respectively. The 3D far-field scattering patterns and the 2D results depicted in blue solid lines are achieved through the simulation of the metasurface structure. While the 2D results depicted in red dashed lines are calculated using the 2D IDFT algorithm.

Now we give the calculation of the spectral response characteristics on different scattering directions of the designed PGM. The azimuth angle of the scattering field main lobe is $\varphi = 0°$, then the 2D IDFT result along the $+k_x$-axis is extracted, as shown in Fig. 6(b). The abscissa of Fig. 6(b) represent the parallel wave vector component $\boldsymbol{k}_{||} = k_0 \sin\theta = 2\pi f \sin\theta/c$, which can be transformed to frequency simply by means of dividing $\boldsymbol{k}_{||}$ by $2\pi \sin\theta/c$. Four direction of $\varphi = 0°$ and $\theta = 50°$, $40°$, $30°$ and $20°$ were taken as examples, the spectral response characteristics are shown in Fig. 7. The amplitude results are normalized by the maximum value of the spectral response in the whole spatial range. It's clearly shown that the 4 spectrums have the similar shape, but different main lobe frequencies. That is to say, due to

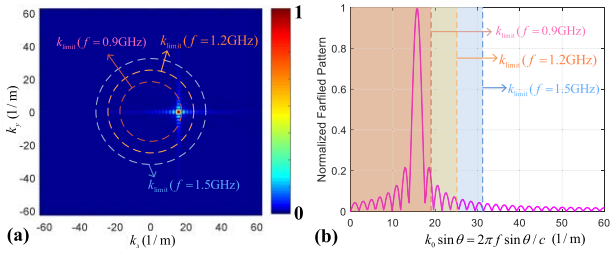

FIGURE 6. (a) 2D DFT result of the PGM structure consists of 64 × 64 unit cells designed in Fig. 4(a). The dashed circles refer to the range of the corresponding k space in the transformation to far-field scatterings for different frequencies. (b) Spectral characteristics of the reflected waves with the same azimuth angle $\varphi = 0°$.

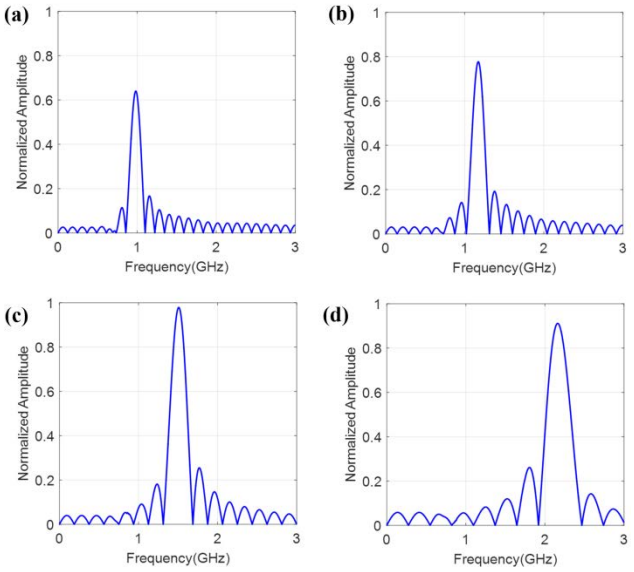

FIGURE 7. Bistatic scattering amplitude spectral response on direction of $\varphi = 0°$and (a) $\theta = 50°$. (b) $\theta = 40°$. (c) $\theta = 30°$.(d) $\theta = 20°$. The amplitude results are normalized by the maximum value of the amplitude spectral response in the whole spatial range.

the chromatic dispersion effect on PGM, waves with different frequencies are received on different directions.

IV. BISTATIC RADAR SIGNAL MODULATION

As mentioned above, the designed PGM generated different spectral response characteristics at different directions. For a wideband incidence, scattered waves no longer carry complete information of the transmitted waves, in other words, there was a distortion for the EM signal. In the above situation of normal incidence, reflections are in different directions with the incidences. That has impact on the structure's bistatic radar scattering characteristic. Here, we take a typical wideband radar system to study the signal characteristic of scatterings.

Linear frequency modulation (LFM) signal is a typical kind of pulse compression signal, which has been widely used in modern radar systems. It can enhance the signal noise ratio (SNR) of radar receiver and has high distance resolution at the same time [34]. The transmitted LFM pulse signal can be expressed as

$$s_0(t) = A_0 \cos(2\pi f_0 t + \pi \mu t^2)\text{rect}\,(t/T) \tag{7}$$

in which A_0 is the peak amplitude, f_0 =1.0GHz is the carrier frequency, $\mu = 3 \times 10^{14}\text{s}^{-2}$ is the frequency modulation slope and T = 2us is pulse width. The rectangular window function rect(t/T)=1 for $0 \le t \le$ T and rect(t/T)=0 otherwise. The bandwidth of LFM signal can be calculated as $B = \mu T$ = 0.6GHz. The base band waveform and the spectrum of the transmitted signal are shown in Fig. 8. It is worth noting that the spectrum of the LFM signal has a shape very close to rectangle, which covers the frequency range from 1.0GHz to 1.6GHz.

For normal simple stationary target without metasurafce structure, the echo signal had experienced attenuation of the amplitude and time delay, which can be expressed as [34]

$$\begin{aligned} e_1(t) = A_1 \cos[2\pi f_0(t - T_1) + \pi\mu(t - T_1)^2] \\ \times \text{rect}[(t - T_1)/T] \end{aligned} \tag{8}$$

where A_1 is the echo amplitude, $T_1 = 2R_1/\text{c}$, is the delay time, here R_1 and c represents the target distance and the light velocity, respectively. Obviously, the echo has the same waveform with the source, they are highly correlated.

While for the designed metasurface target, the echo gets strong distortion. The distorted echo spectrum $S_2(f)$ can be calculated as multiplication of the normal echo $S_1(f)$ and the spectral response $r(f)$ which has been got in Section III.

$$S_2(f) = S_1(f)r(f) \tag{9}$$

Then the waveform of the distorted echo can be got from the inverse Fourier transform of $S_2(f)$.

$$e_2(t) = \frac{1}{2\pi}\int_{-\infty}^{\infty} S_2(f)e^{j2\pi ft}df \tag{10}$$

In order to evaluate the modulation effect, the echoes in 4 different directions were calculated and shown in Fig. 9-12. The results indicate that both the waveforms and spectrums are distorted besides the amplitude attenuation. Corresponding to the reflectance in Fig. 7(a), where the main peak is located nearly 1.0GHz, Fig. 9 shows the echo at $\theta = 50°$, the spectrum of the bistatic scattering signal no more like a rectangle, but turned out to be a sharp main peak at 1.0GHz with several side peaks following on the right. Meanwhile, the waveform was no longer a normal rectangle pulse, but broken up into several little pieces with ups and downs amplitude. These special effect are result from the impact of the metasurface.

Corresponding to Fig. 7(b), where the main peak in located near 1.2GHz, Fig. 10 shows the echo at $\theta = 40°$, the spectrum of the bistatic scattering signal also no more like a rectangle, but turned out to be a main peak near 1.2GHz with two side peaks following on the right side. Also, the waveform was broken up into several little pieces with ups and downs amplitude.

Corresponding to Fig. 7(c), where the main peak is located near 1.5GHz, Fig. 11 shows the echo at $\theta = 30°$, the spectrum

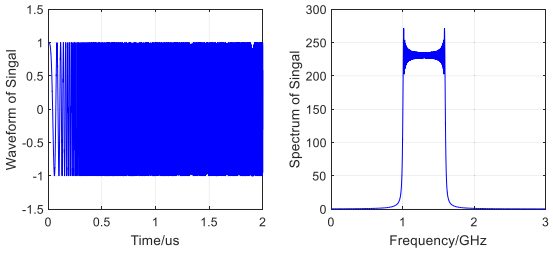

FIGURE 8. (a) Time-domain waveform of the transmitted wideband LFM wave. (b) Spectrum of the transmitted LFM wave.

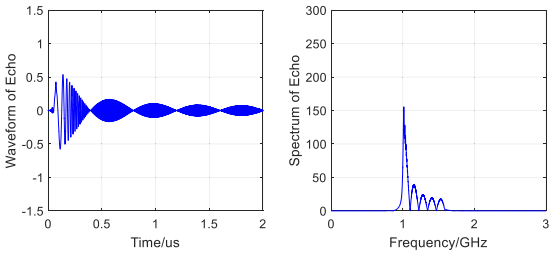

FIGURE 9. (a) Time-domain waveform of the bistatic echo scattered into $\theta = 50°$. (b) Spectrum of the echo scattered into $\theta = 50°$.

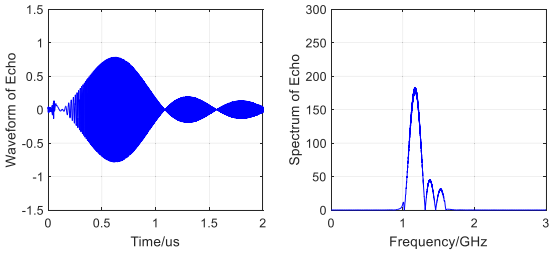

FIGURE 10. (a) Time-domain waveform of the bistatic echo scattered into $\theta = 40°$. (b) Spectrum of the echo scattered into $\theta = 40°$.

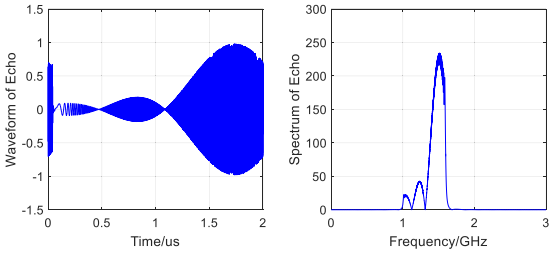

FIGURE 11. (a) Time-domain waveform of the bistatic echo scattered into $\theta = 30°$. (b) Spectrum of the echo scattered into $\theta = 30°$.

of the bistatic scattering signal also no more like a rectangle, but turned out to be a main peak near 1.5GHz with two side peaks lying on the left side. Also, the waveform was broken up into several little pieces with ups and downs amplitude.

Corresponding to Fig. 7(d), where the main peak is located near 2.2GH, outside the band of the transmitted LFM signal, Fig. 12 shows the echo at $\theta = 20°$, the spectrum of the bistatic scattering signal has no clear main peak, but turned out to be several tiny peaks ranging one by one. This is because the spectrum of the incidence was responded by the side lobe of the bistatic scattering spectrum. Simultaneously, the scattered energy was less than the other in-band response situations.

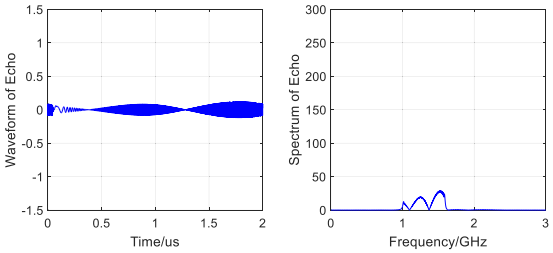

FIGURE 12. (a) Time-domain waveform of the bistatic echo scattered into $\theta = 20°$. (b) Spectrum of the echo scattered into $\theta = 20°$.

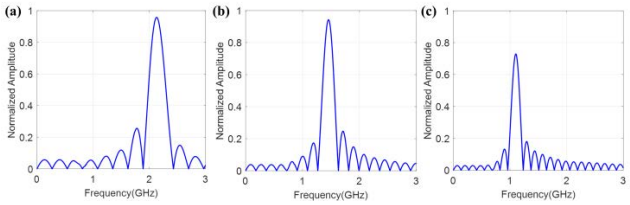

FIGURE 13. Monostatic scattering amplitude spectrum response on direction of $\varphi = 0°$ and (a) $\theta = 10°$. (b) $\theta = 15°$. (c) $\theta = 20°$.

In general, the metasurface-scattered waves in different directions were all seriously distorted, no longer carry the whole information of the transmitter. It is easy to assume that due to the waveform and spectrum distortion, the chromatic dispersion in PGM will lower down the ability of radar detection.

V. MONOSTATIC RADAR SIGNAL MODULATION AND THE JAMMING EFFECTIVENESS

In this section, we continue to talk about the monostatic scattering characteristics and its jamming effectiveness on radar detection. Monostatic radar is a type of widely used radar system whose transmitter and receiver are located at the same place. For the detected target, the directions of the received and transmitted waves are identical, i.e. $\theta_r = \theta_i$, $\varphi_r = \varphi_i$. So the calculation of the scattered field is not the situation of normal incidence, which now meets the relations $k_{xr} = k_{xi}$, $k_{yr} = k_{yi}$. Here we take three different directions ($\theta_r = \theta_i = 10°, 15°, 20°$) as representatives, the calculated spectral response on the three directions are shown in Fig. 13, the corresponding echoes are shown in Fig. 14, Fig. 15 and Fig. 26, respectively.

As shown in Fig. 13(a), the main peak is located near 2.16GH, outside the frequency band of the transmitted LFM signal. Fig. 14 shows the monostatic echo at $\theta = 10°$, the spectrum of the scattering signal has no clear main peak, but turned out to be several tiny peaks. This is because the spectrum of the incidence was responded by the side lobe of the monostatic scattering spectrum.

As shown in Fig. 13(b), the main peak is located near 1.45GHz. Fig. 15 shows the monostatic echo at $\theta = 15°$, the spectrum of the scattering signal no more like a rectangle, but turned out to be a main peak near 1.45GHz with two side peaks lie on the left side. Meanwhile, the waveform

was broken up into several little pieces with ups and downs amplitude.

As shown in Fig. 13(c), the main peak is located nearly 1.10GHz, Fig. 16 shows the monostatic echo at $\theta = 20°$, the spectrum of the scattering signal also no more like a rectangle, but turned out to be a main peak near 1.10GHz with several side peaks following on the right side. Also, the waveform is no longer a normal rectangle pulse, but broken up into several little pieces with ups and downs amplitude.

It can be confirmed that due to the chromatic dispersion in PGM, the echoes got great distortion for both waveforms and spectrums. This distortion will result in mismatch between the radar echo and the transmitted signal, reduction of the SNR in the matched filter, and then lowering down the radar detection [38], [39].

Then, we further evaluated the jamming effectiveness on monostatic radar system according to the principle of correlation detection. To improve the ability of radar detect, matched filters are always used to do correlation detection. The output of the matched filter can be got by the cross-correlation function of the transmitted signal and the echo.

$$y(t) = \int_{-\infty}^{\infty} e_2(\tau) s_0(t-\tau) d\tau \tag{11}$$

Common radar echo carries similar waveform with the transmitted signal, they have strong correlation. Coherent accumulation improve radar target recognition probability in common conditions. However, as talked above, the echo scattered by PGM gets great distortion for both waveforms and spectrums, which will lower down the correlation between the echo and the original signal.

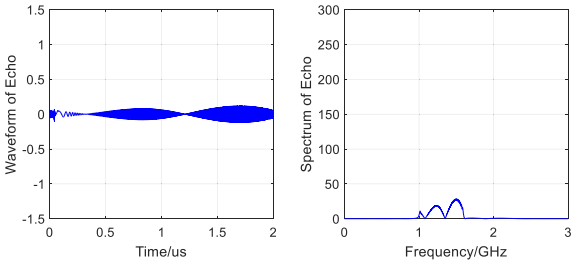

FIGURE 14. Monostatic scattering signal. (a) Time-domain waveform of the echo scattered into $\theta = 10°$. (b) Spectrum of the echo scattered into $\theta = 10°$.

We calculated the one dimensional range profile of the above mentioned three monostatic radar echoes after the processing of matched filter, the results with and without PGM are shown from Fig. 17 to Fig. 19, respectively.

Corresponding to Fig. 14, whose main peak of the spectrum are located outside the signal band, Fig. 17 shows the results of the matched filter for $\theta = 10°$. The output energy of the matched filter got a great loss of 15.5dB. What is more, the distance deviated more than 7m from the real location of the target. And the resolution got worse as the output signal of the target got broader and no more smooth, as the main lobe of blue line shown in Fig. 22.

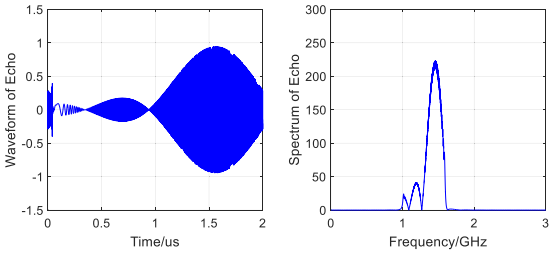

FIGURE 15. Monostatic scattering signal. (a) Time-domain waveform of the echo scattered into $\theta = 15°$. (b) Spectrum of the echo scattered into $\theta = 15°$.

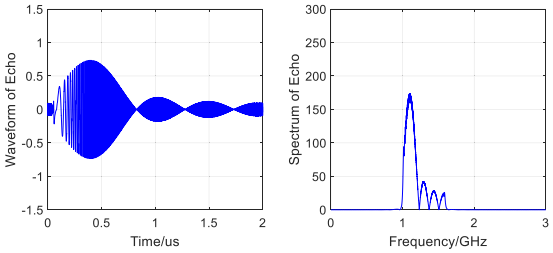

FIGURE 16. Monostatic scattering signal. (a) Time-domain waveform of the echo scattered into $\theta = 20°$. (b) Spectrum of the echo scattered into $\theta = 20°$.

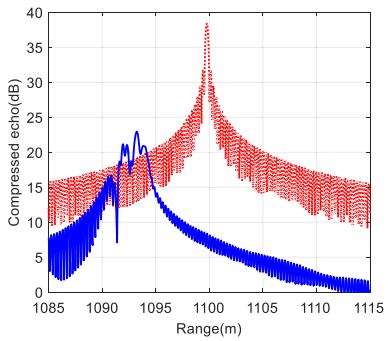

FIGURE 17. Matched filter results with (red dashed line) and without (blue solid line) metamaterial for $\theta = 10°$.

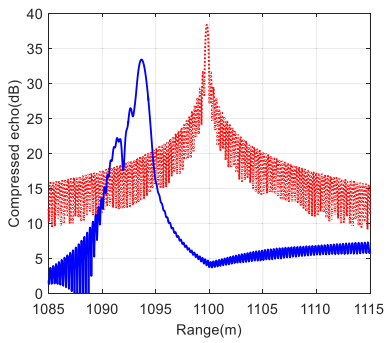

FIGURE 18. Matched filter results with (red dashed line) and without (blue solid line) metamaterial for $\theta = 15°$.

Corresponding to Fig. 15 and Fig. 16, the main peaks of the spectrum are located within the signal band, Fig. 18 and Fig. 19 show the results of the matched filter for $\theta = 15°$ and $\theta = 20°$, respectively. The output energy of the matched filter got loss of 5.0dB and 7.6dB, respectively. Also, the distance

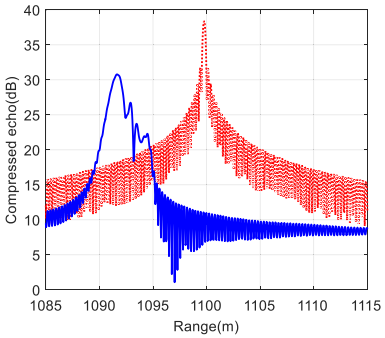

FIGURE 19. Matched filter results with (red dashed line) and without (blue solid line) metamaterial for $\theta = 20°$.

deviate from the real location of the target, and the resolution got worse. That is to say, the function of the PGM not only lower down the correlation of the echo, but also hide the real location of the target. These special jamming effect may provide additional advantages in the radar countermeasure.

VI. CONCLUSION

In conclusion, we analyzed the chromatic dispersion on PGMs and its influence on the spectral response in different scattering directions. The far-field scattering pattern was obtained by calculating the 2D Fourier transform of the phase pattern on metasurface. Then the direction-related spectral response was got in the 2D wave vector space. Furthermore, the wideband LFM signal was taken as an example, its bistatic and monostatic scatter's waveform and spectral characteristics were studied. The results shown that the scattered signals were greatly distorted, causing the correlation reduction and range deviation in radar detection process. We remark that this signal modulation mechanism on PGMs is based on the material-level response, possess speed advantage over traditional signal modulation circuits; it may propose potential applications in signal processing, radar countermeasures, new communication and antennas systems, etc.

REFERENCES

[1] A. V. Kildishev, A. Boltasseva, and V. M. Shalaev, "Planar photonics with metasurfaces," *Science*, vol. 339, no. 6125, Mar. 2013, Art. no. 1232009.
[2] N. Yu and F. Capasso, "Flat optics with designer metasurfaces," *Nature Mater.*, vol. 13, no. 2, pp. 139–150, Jan. 2014.
[3] S. M. Kamali, E. Arbabi, A. Arbabi, and A. Faraon, "A review of dielectric optical metasurfaces for wavefront control," *Nanophotonics*, vol. 7, no. 6, pp. 1041–1068, Jun. 2018.
[4] S. Sun, Q. He, J. Hao, S. Xiao, and L. Zhou, "Electromagnetic metasurfaces: Physics and applications," *Adv. Opt. Photon.*, vol. 11, no. 2, pp. 380–479, Jun. 2019.
[5] F. Ding, Y. Yang, R. A. Deshpande, and S. I. Bozhevolnyi, "A review of gap-surface plasmon metasurfaces: Fundamentals and applications," *Nanophotonics*, vol. 7, no. 6, pp. 1129–1156, Jun. 2018.
[6] N. M. Estakhri and A. Alù, "Recent progress in gradient metasurfaces," *J. Opt. Soc. Amer. B, Opt. Phys.*, vol. 33, no. 2, pp. A21–A30, Feb. 2016.
[7] N. Yu, P. Genevet, M. A. Kats, F. Aieta, J. P. Tetienne, F. Capasso, and Z. Gaburro, "Light propagation with phase discontinuities: Generalized laws of reflection and refraction," *Science*, vol. 334, no. 6054, pp. 333–337, Oct. 2011.
[8] F. Aieta, P. Genevet, N. Yu, M. A. Kats, Z. Gaburro, and F. Capasso, "Out-of-plane reflection and refraction of light by anisotropic optical antenna metasurfaces with phase discontinuities," *Nano Lett.*, vol. 12, no. 3, pp. 1702–1706, Mar. 2012.
[9] Y. Fan, J. Wang, H. Ma, J. Zhang, D. Feng, M. Feng, and S. Qu, "In-plane feed antennas based on phase gradient metasurface," *IEEE Trans. Antennas Propag.*, vol. 64, no. 9, pp. 3760–3765, Sep. 2016.
[10] H. Li, G. Wang, H.-X. Xu, T. Cai, and J. Liang, "X-band phase-gradient metasurface for high-gain lens antenna application," *IEEE Trans. Antennas Propag.*, vol. 63, no. 11, pp. 5144–5149, Nov. 2015.
[11] J.-J. Liang, G.-L. Huang, J.-N. Zhao, Z.-J. Gao, and T. Yuan, "Wideband phase-gradient metasurface antenna with focused beams," *IEEE Access*, vol. 7, pp. 20767–20772, 2019.
[12] J. Wang, S. Qu, Z. Xu, H. Ma, X. Wang, D. Huang, and Y. Li, "Superthin cloaks mediated by spoof surface plasmons," *Photon. Nanostruct., Fundam. Appl.*, vol. 10, no. 4, pp. 540–546, Oct. 2012.
[13] Y. Cheng, C. Wu, C. Ge, J. Yang, X. Pei, F. Jia, and R. Gong, "An ultra-thin dual-band phase-gradient metasurface using hybrid resonant structures for backward RCS reduction," *Appl. Phys. B, Lasers Opt.*, vol. 123, p. 143, May 2017.
[14] S. Sun, Q. He, S. Xiao, Q. Xu, X. Li, and L. Zhou, "Gradient-index metasurfaces as a bridge linking propagating waves and surface waves," *Nature Mater.*, vol. 11, no. 5, pp. 426–431, May 2012.
[15] W. Sun, Q. He, S. Sun, and L. Zhou, "High-efficiency surface plasmon meta-couplers: Concept and microwave-regime realizations," *Light, Sci. Appl.*, vol. 5, no. 1, Jan. 2016, Art. no. e16003.
[16] S. Taravati and G. V. Eleftheriades, "Programmable nonreciprocal metaprism," *Sci. Rep.*, vol. 11, no. 1, p. 7377, Dec. 2021.
[17] D. Dardari and D. Massari, "Using metaprisms for performance improvement in wireless communications," *IEEE Trans. Wireless Commun.*, vol. 20, no. 5, pp. 3295–3307, May 2021.
[18] M. Born and E. Wolf, *Principles of Optics: Electromagnetic Theory of Propagation, Interference and Diffraction of Light*, 7th ed. Cambridge, U.K.: Cambridge Univ. Press, 1999.
[19] J. W. Goodman, *Introduction to Fourier Optics*, 3rd ed. Englewood, CO, USA: Roberts and Company, 2005.
[20] M. Faraji-Dana, E. Arbabi, A. Arbabi, S. M. Kamali, H. Kwon, and A. Faraon, "Compact folded metasurface spectrometer," *Nature Commun.*, vol. 9, no. 1, p. 4196, Oct. 2018.
[21] A. McClung, M. Mansouree, and A. Arbabi, "At-will chromatic dispersion by prescribing light trajectories with cascaded metasurfaces," *Light, Sci. Appl.*, vol. 9, no. 1, p. 93, May 2020.
[22] W. Zang, Q. Yuan, R. Chen, L. Li, T. Li, X. Zou, G. Zheng, Z. Chen, S. Wang, Z. Wang, and S. Zhu, "Chromatic dispersion manipulation based on metalenses," *Adv. Mater.*, vol. 32, no. 27, Dec. 2019, Art. no. 1904935.
[23] F. Aieta, M. A. Kats, P. Genevet, and F. Capasso, "Multiwavelength achromatic metasurfaces by dispersive phase compensation," *Science*, vol. 347, no. 6228, pp. 1342–1345, Mar. 2015.
[24] W. Chen, A. Y. Zhu, V. Sanjeev, M. Khorasaninejad, Z. Shi, E. Lee, and F. Capasso, "A broadband achromatic metalens for focusing and imaging in the visible," *Nature Nanotechnol.*, vol. 13, no. 3, pp. 220–226, Mar. 2018.
[25] W. T. Chen, A. Y. Zhu, J. Sisler, Z. Bharwani, and F. Capasso, "A broadband achromatic polarization-insensitive metalens consisting of anisotropic nanostructures," *Nature Commun.*, vol. 10, no. 1, p. 355, Jan. 2019.
[26] B. Lin, J. Guo, L. Lv, Z. Liu, X. Ji, and J. Wu, "An ultra-wideband reflective phase gradient metasurface using Pancharatnam–Berry phase," *IEEE Access*, vol. 7, pp. 13317–13325, 2019.
[27] Z. Chen, H. Deng, Q. Xiong, and C. Liu, "Phase gradient metasurface with broadband anomalous reflection based on cross-shaped units," *Appl. Phys. A, Solids Surf.*, vol. 124, no. 3, Mar. 2018, Art. no. 281.
[28] W. Zhang, Y. Liu, S. Gong, J. Wang, and Y. Jiang, "Wideband RCS reduction of a slot array antenna using phase gradient metasurface," *IEEE Antennas Wireless Propag. Lett.*, vol. 17, no. 12, pp. 2193–2197, Dec. 2018.
[29] J. Xu, B. Bai, C. Dong, Y. Dong, Y. Zhu, and G. Zhao, "Evaluations of plasma stealth effectiveness based on the probability of radar detection," *IEEE Trans. Plasma Sci.*, vol. 45, no. 6, pp. 938–944, Jun. 2017.
[30] J. Xu, B. Bai, C. Dong, and G. Zhao, "A novel passive jamming method against ISAR based on resonance absorption effect of metamaterials," *IEEE Access*, vol. 6, pp. 18142–18148, 2018.
[31] J. Wang, D. Feng, L. Xu, R. Zhang, and W. Hu, "Synthetic aperture radar target feature modulation using active frequency selective surface," *IEEE Sensors J.*, vol. 19, no. 6, pp. 2113–2125, Mar. 2019.
[32] Z. Wang, J. Wang, H. Ma, X. Wang, Y. Meng, J. Zhang, Y. Zhang, and S. Qu, "High-efficiency real-time waveform modulator for free space waves based on dispersion engineering of spoof surface plasmon polaritons," *J. Phys. D, Appl. Phys.*, vol. 50, no. 21, Jun. 2017, Art. no. 215104.

[33] Q. Zheng, Y. Li, J. Zhang, H. Ma, J. Wang, Y. Pang, Y. Han, S. Sui, Y. Shen, H. Chen, and S. Qu, "Wideband, wide-angle coding phase gradient metasurfaces based on Pancharatnam–Berry phase," *Sci. Rep.*, vol. 7, no. 1, p. 43543, Mar. 2017.
[34] M. A. Richards, *Fundamentals of Radar Signal Processing*. New York, NY, USA: McGraw-Hill, 2005.
[35] J. W. Goodman, *Introduction to Fourier Optics*, 3rd ed. Englewood, CO, USA: Roberts and Company, 2004.
[36] T. J. Cui, M. Q. Qi, X. Wan, J. Zhao, and Q. Cheng, "Coding metamaterials, digital metamaterials and programmable metamaterials," *Light, Sci. Appl.*, vol. 3, no. 10, p. e218, Oct. 2014.
[37] H.-X. Xu, G.-M. Wang, T. Cai, J. Xiao, and Y. Q. Zhuang, "Tunable Pancharatnam–Berry metasurface for dynamical and high-efficiency anomalous reflection," *Opt. Exp.*, vol. 24, no. 24, pp. 27836–27848, Nov. 2016.
[38] D. O. North, "An analysis of the factors which determine signal/noise discrimination in pulsed-carrier systems," *Proc. IEEE*, vol. 51, no. 7, pp. 1016–1027, Jul. 1963.
[39] G. Q. Zhao, *Principle of Radar Countermeasure*. Xi'an, China: Xidian Univ. Press, 2012.

YUEYU MENG received the B.S. degree in electronic countermeasures engineering, the M.S. degree in information and communication engineering, and the Ph.D. degree in physical electronics form Air Force Engineering University, Xi'an, Shaanxi, China, in 2012, 2014, and 2018, respectively.

He has been with the Fundamentals Department, Air Force Engineering University, since 2018. His current research interests include electronic countermeasures, metamaterials, and spoof surface plasmon polaritons.

JIAFU WANG (Member, IEEE) received the B.S. degree in radar engineering, the M.S. degree in optics engineering, the Ph.D. degree in physical electronics from Air Force Engineering University, Xi'an, Shaanxi, China, in 2004, 2007, and 2010, respectively.

He has been with Air Force Engineering University, since 2010. His current research interests include plasma stealth, and design and application of the metamaterials in microwave devices.

WEIYU WANG received the M.S. degree in optics engineering from Air Force Engineering University, Xi'an, Shaanxi, China, in 2013. He has been with Air Force Engineering University, since 2013. His current research interests include optics and infrared physics.

LIN ZHENG received the Ph.D. degree in electronics science and technology from Air Force Engineering University, Xi'an, Shaanxi, China, in 2015. He is currently with the School of Information and Communications Engineering, Xi'an Jiaotong University. His research interests include frequency selective surface and metamaterials.

YONGFENG LI, photograph and biography not available at the time of publication.

HUA MA received the B.S. degree in physics from the National University of Defense Technology, Changsha, Hunan, China, in 1997, the M.S. degree in optics engineering from Xi'an Electronic and Technology University, Xi'an, Shaanxi, China, in 2006, and the Ph.D. degree in physical electronics from Air Force Engineering University, Xi'an, in 2009.

He has been with Air Force Engineering University, since 1997. His research interests include the characteristics of photonic crystals and the design of metamaterials.

SHAOBO QU received the B.S. degree in physics from Fuyang Normal College, Fuyang, Anhui, China, in 1984, the M.S. degree in physics from Sichuan Normal University, Chengdu, China, in 1991, and the Ph.D. degree in materials science and engineering from Northwest Polytechnical University, Xi'an, China, in 2001.

Since 2001, he has been with the Department of Applied Mathematics and Physics, Air Force Engineering University, Xi'an, where he is currently a Professor of physical electronics. His research interests include materials physics, metamaterials, and electronic materials and devices.